Cancer-associated fibroblasts of the prostate promote a compliant and more invasive phenotype in benign prostate epithelial cells

A. Jaeschke [a,b], A. Jacobi [c,d], M.G. Lawrence [e,f,g], G.P. Risbridger [e,f,g], M. Frydenberg [e,h,i], E.D. Williams [a,j,k,l], I. Vela [a,j,k,l,m], D.W. Hutmacher [a,b,l], L.J. Bray [a,b,*,n], A. Taubenberger [c,n]

[a] Institute of Health and Biomedical Innovation, Queensland University of Technology (QUT), Kelvin Grove, Australia
[b] School of Mechanical, Medical and Process Engineering, Science and Engineering Faculty, Queensland University of Technology (QUT), Brisbane, Australia
[c] Biotechnology Center, Technische Universität Dresden, Germany
[d] Max Planck Institute for the Science of Light & Max-Planck-Zentrum für Physik und Medizin, Erlangen, Germany
[e] Monash Biomedicine Discovery Institute Cancer Program, Prostate Cancer Research Group, Department of Anatomy and Developmental Biology, Monash University, Clayton, Victoria, Australia
[f] Cancer Research Division, Peter MacCallum Cancer Centre, Melbourne, Victoria, Australia
[g] Sir Peter MacCallum Department of Oncology, The University of Melbourne, Parkville, Victoria, Australia
[h] Australian Urology Associates, Melbourne, Victoria, Australia
[i] Department of Urology, Cabrini Health, Malvern, Victoria, Australia
[j] Australian Prostate Cancer Research Centre-Queensland, Queensland University of Technology (QUT), Kelvin Grove, Australia
[k] Translational Research Institute, Woolloongabba, Australia
[l] School of Biomedical Sciences, Faculty of Health, Queensland University of Technology (QUT), Brisbane, Australia
[m] Department of Urology, Princess Alexandra Hospital, Woolloongabba, Australia

ARTICLE INFO

ABSTRACT

Reciprocal interactions between prostate epithelial cells and their adjacent stromal microenvironment not only are essential for tissue homeostasis but also play a key role in tumor development and progression. Malignant transformation is associated with the formation of a reactive stroma where cancer-associated fibroblasts (CAFs) induce matrix remodeling and thereby provide atypical biochemical and biomechanical signals to epithelial cells. Previous work has been focused on the cellular and molecular phenotype as well as on matrix stiffness and remodeling, providing potential targets for cancer therapeutics. So far, biomechanical changes in CAFs and adjacent epithelial cells of the prostate have not been explored. Here, we compared the mechanical properties of primary prostatic CAFs and patient-matched non-malignant prostate tissue fibroblasts (NPFs) using atomic force microscopy (AFM) and real-time deformability cytometry (RT-FDC). It was found that CAFs exhibit an increased apparent Young's modulus, coinciding with an altered architecture of the cytoskeleton compared with NPFs. In contrast, co-cultures of benign prostate epithelial (BPH-1) cells with CAFs resulted in a decreased stiffness of the epithelial cells, as well as an elongated morphological phenotype, when compared with co-cultures with NPFs. Moreover, the presence of CAFs increased proliferation and invasion of epithelial cells, features typically associated with tumor progression. Altogether, this study provides novel insights into the mechanical interactions between epithelial cells with the malignant prostate microenvironment, which could potentially be explored for new diagnostic approaches.

1. Introduction

Prostate cancer (PCa) is the second most common cancer in men worldwide and a leading cause of cancer deaths [1]. While survival rates for the localized disease are high, once the cancer metastasizes, the prognosis worsens drastically [2]. Therefore, a greater understanding of the mechanisms driving cancer progression is imperative. Numerous studies have suggested an essential role of the microenvironment in tumor development and progression [3–7]. The prostate epithelium, where prostate adenocarcinomas arise, is enclosed in a complex

---

* Corresponding author.
  E-mail address: laura.bray@qut.edu.au (L.J. Bray).
[n] These authors share senior authorship.

microenvironment comprising a variety of other cell types such as smooth muscle, fibroblasts, vascular, and immune cells as well as autonomic nerve fibers [5]. Fibrous proteins, mainly collagen, elastin, fibronectin and laminin, and proteoglycans constitute the extracellular matrix (ECM) [8,9]. The stromal microenvironment provides a physiological framework, encompassing physical support combined with biochemical factors needed for normal development, growth, and homeostasis of the epithelium. Disturbances in reciprocal interactions between epithelial cells and the surrounding stroma contribute to PCa progression [10]. Typically, malignant transformation is associated with an altered stromal microenvironment, characterized by changes in cellular composition, ECM remodeling and growth factor availability [5, 11,12]. A fundamental component of the tumor stroma are cancer-associated fibroblasts (CAFs). Paracrine signals from the stroma enhance cell proliferation and induce tumorigenesis in the epithelium [13,14]. Reciprocally, cancerous cells secrete growth factors involved in fibroblast activation [15]. Besides the biochemical signals, biomechanical and topographical cues are essential for the interactions between the fibroblasts and the epithelium. CAFs alter the tumor microenvironment through increased deposition and remodeling of ECM molecules [16]. The resulting changes in fiber formation and alignment promote invasion and migration of tumor cells and contribute to cancer progression [17–20]. Previous studies investigating the mechanical characteristics of prostate tissue sections revealed an increased stiffness of cancerous tissue compared with healthy tissue [21–23]. Besides, CAF-derived acellular matrices from head and neck cancer patients had increased elastic modulus compared with matrices from normal fibroblasts [19].

Paradoxically, the elastic properties of cancerous tissue and malignant cells appear to be inversely related. Epithelial PCa cell lines are typically more compliant than normal or benign cells [24,25], consistent with studies of other types of cancer cells [26–28]. Moreover, decreased cell stiffness is associated with enhanced migratory and invasive capacity of epithelial cells [29–31].

Different methods have been used to measure the mechanical properties of cells, including micropipette aspiration, magnetic beads, microneedles, and optical stretchers [32,33]. The gold standard is atomic force microscopy (AFM)–based cell indentation, which has the benefit of being used for both spread and rounded cells as well as tissues [34]. Over the past years, high-throughput methods have also been developed for measuring cell mechanical properties. Among them, real-time deformability cytometry (RT-FDC) is based on the hydrodynamic deformation of single cells moving through a microfluidic [35].

In this study, we compared the mechanical properties of primary CAFs and non-malignant prostate tissue fibroblasts (NPFs) isolated from malignant or benign regions of prostate tissue from the same patient [36]. Previous works have identified distinct proteomic and epigenetic profiles in patient-matched pairs of stromal cells, altered interactions with epithelial and immune cells, as well as aberrant ECM deposition, compared with normal fibroblasts from the prostate [17,37–41]. Here, we compare the mechanical characteristics of patient-matched CAFs and NPFs as well as their co-cultures with benign prostatic epithelial cells using AFM and RT-FDC. Besides changes in the ECM and the cytoskeleton, distinct mechanical phenotypes of CAFs and NPFs are revealed, with CAF cultures being stiffer compared with NPFs. In return, on co-cultures, benign prostatic epithelial cells became more compliant, which coincided with a more invasive and proliferative phenotype.

2. Materials and methods

2.1. Primary prostatic fibroblasts

Fresh patient tissues were collected from radical prostatectomy specimens with written informed consent from patients. These studies were approved by Human Research Ethics Committees at Monash University (2004/145) and Cabrini Hospital (03-14-04-08) in Melbourne, Australia. Primary cultures of CAFs were established from tumor tissue and matched NPFs from non-malignant tissue as previously described [36]. A board-certified pathologist confirmed that the tumor tissue contained approximately 80% cancer and that the non-malignant tissue was benign. Cells were maintained in RPMI 1640 media (no phenol red; Gibco, ThermoFisher) supplemented 5% fetal bovine serum (FBS; Gibco, ThermoFisher), 1 nM testosterone (Sigma-Aldrich), 10 ng/mL human fibroblast growth factor 2 (hFGF-2; Miltenyi Biotec), 100 U/mL penicillin, and 100 μg/mL streptomycin (Gibco, ThermoFisher). Cells were maintained at 37 °C in 5% CO_2, with media changes every 2–3 days. Matched fibroblasts from two patients were used for this study between passages 5 and 8.

2.2. Histological analysis of prostate tissue

Samples of prostate tissue were retained from each patient specimen. The tissues were formalin fixed, paraffin embedded, cut into 5 μm sections, and mounted onto Superfrost microscope slides (ThermoFisher). The sections were dewaxed, stained with hematoxylin (Amber Scientific, Australia) for 60 s, rinsed with hot tap water, and counterstained with eosin (Amber Scientific) for 45 s, dehydrated, and mounted with Dibutylphthalate Polystyrene Xylene (DPX; Merck).

2.3. Benign prostate epithelial-1 cell culture

Benign prostate epithelial (BPH-1) cells were kindly provided by the Australian Prostate Cancer Research Centre Queensland. The BPH-1 cell line was fluorescently labelled for tracking purposes as previously described [42]. Briefly, the cell line was incubated overnight with an in-house-generated GFP lentivirus with polybrene (8 μg/mL). GFP-positive BPH-1 cells were selected using a BD FACSAria Fusion cell sorter (BD Biosciences). GFP-tagged BPH-1 cells were maintained in RPMI 1640 media (no phenol red), supplemented with 5% FBS, 100 U/mL penicillin, and 100 μg/mL streptomycin at 37 °C, 5% CO_2.

2.4. Epithelial-fibroblast co-culture

NPFs or CAFs were seeded at 1.58×10^4 cells/cm^2 onto Thermanox coverslips (Ø 13 mm; Nunc, ThermoFisher) in 24 well plates (Nunc, ThermoFisher). Cells were cultured in fibroblast medium at 37 °C, 5% CO_2 and after 24 h the medium was supplemented with 50 μg/mL ascorbic acid (Sigma) to stimulate ECM deposition [43]. Fibroblasts were cultured for a further 5 days to yield a dense monolayer and ECM deposition. Then BPH-1 cells were seeded on top of the fibroblasts at a density of 2.11×10^4 cells/cm^2. The co-culture was cultivated in fibroblast medium at 37 °C, 5% CO_2 for 48 h.

2.5. Immunofluorescence

Samples were fixed with 4% paraformaldehyde (Sigma) for 12 min at room temperature (RT) and washed twice with PBS (Oxoid). Cells were permeabilized in PBS supplemented with 0.1% Triton-X100 (Merck) and blocked with 5% goat serum (Gibco, ThermoFisher) for 1 h at RT. Thereafter, samples were incubated with the primary antibody diluted in 1% goat serum for 1 h at RT. After washing with 0.05% Tween-20 (Merck) in PBS, samples were incubated with the fluorescently labelled secondary antibody, phalloidin and 5 μg/mL 4′,6-diamidino-2-phenylindole (DAPI; Invitrogen, ThermoFisher) diluted in 1% goat serum in PBS. Further information on the primary and secondary antibodies and their dilutions is listed in Supplementary Table S1. After washing with PBS and distilled H_2O (Sartorius), the samples were mounted upside down onto thin glass coverslips (No. 1, Hurst Scientific) using Prolong Gold (Invitrogen, ThermoFisher). Since the samples were imaged through the glass coverslip using an inverted confocal microscope with a pinhole setting of 14 μm, the Thermanox background fluorescence was excluded. Images were acquired on a confocal microscope (Nikon A1R confocal microscope (Nikon Instruments Inc.; 40x,

0.31 μm/px x 0.31 μm/px, z-step size 0.75 μm), or Leica SP5 (Leica Microsystems Pty Ltd; 20x, 0.19 μm/px x 0.19 μm/px, z-step size 1 μm)).

2.6. Release of cells from Thermanox surfaces

Cells in mono- or co-cultures were detached from the Thermanox coverslip to perform measurements on released cells. After washing in PBS for 5 min, the cells were incubated with twice TrypLE (Gibco, ThermoFisher) for 7 min. TrypLE (Gibco, ThermoFisher) was collected after the first incubation. Detached cells were centrifuged at 200 g for 5 min, and after a washing step with PBS, resuspended in PBS.

2.7. Atomic force microscopy

For AFM indentation experiments on BPH-1, CAFs, and NPFs, a Nanowizard 4 (JPK Instruments) was used. Arrow-TL1 cantilevers (Nanoworld) with a nominal spring constant of 0.035–0.050 N/m that had been equipped with a polystyrene bead of 5 μm diameter (microparticles GmbH) were calibrated by the thermal noise method using built-in procedures of the AFM software. CAF and NPF monocultures and co-cultures with BPH-1 cells were probed as an intact monolayer. Therefore, a cell-carrying Thermanox disc was mounted onto a glass bottom dish (WPI) using vacuum grease (Dow Corning) and gently rinsed with CO_2-independent medium (Gibco, ThermoFisher). The cantilever/bead was positioned over a cell, and four spots per cell area were probed using an approach/retraction speed of 5 μm/s and a relative set point of 2.5 nN.

For the analysis of BPH-1 cells, co-cultures were released from Thermanox surfaces as described above, resuspended in CO_2-independent medium, and kept for 30 min in suspension so that the cells adopted a rounded morphology. Then, the cell suspension was transferred into glass bottom dishes (WPI), to which cells firmly attached within 10 min. BPH-1 cells were discriminated from fibroblasts by their GFP fluorescent signal using epifluorescence microscopy and individually probed using a speed of 5 μm/s and a relative set point of 2.5 nN. All experiments were performed at 37 °C using a petri dish heater (JPK instruments) and in CO_2-independent medium. The resulting force distance curves were analyzed using the JPK image processing software (JPK instruments). Force distance data were corrected for the tip sample separation and fitted with the Hertz/Sneddon model fit for a spherical indenter to extract the apparent Young's modulus [44,45]. For round cells, apparent Young's moduli were corrected as previously described [46]. A Poisson ratio of 0.5 was assumed.

2.8. Real-time deformability cytometry

Real-time deformability cytometry (RT-FDC) measurements were performed as described previously [35,47]. Cells were released from the Thermanox surface as described above. After 30 min incubation at RT, cells were centrifuged at 200 g for 5 min and resuspended in PBS containing 0.5% methylcellulose. A total of 30 μl of sample volume were drawn into a 1 mL syringe and flushed through a 30-μm narrow channel constriction in a microfluidic chip. A total flow rate of 0.16 mL/s (sample flow 0.04 mL/s, sheath flow 0.12 mL/s) was applied for fibroblast monocultures, and 0.32 mL/s (sample flow 0.08 mL/s, sheath flow 0.24 mL/s) for co-cultures. At the end of the channel, the cells are captured by a high-speed camera, and the contour is tracked. From the contour, the cross-sectional area (A) and the deformation ($D = 1 - 2\sqrt{\pi A}/l$, l - perimeter of the contour) are derived. A bright-field image is acquired for every measured cell making the data available for multiparametric offline analysis that allows for the discrimination between different cell types. Data analysis and computation of the apparent elastic modulus was performed in ShapeOut 1.0.10 (available at https://github.com/ZELLMECHANIK-DRESDEN/ShapeOut).

2.9. Protein preparation

Primary CAFs and NPFs were cultured as described above. Cells were detached from the Thermanox™ surface using a cell scraper (Sarstedt) and centrifuged at 200 g for 10 min. After a washing step with PBS, the cell pellet was stored at −20 °C. Cells were lysed by resuspending the pellet in a buffer containing 1% sodium deoxycholate in 100 mM Tris (pH8; Sigma), 10 mM Tris[2-carboxyethyl] phosphine-HCl (TCEP; Sigma), 40 mM 2-chloroacetamide (2CAA; Sigma) followed by a sonication step for 15 min, and an incubation at 95 °C for 5 min. For digestion, the protein solution was mixed with sequencing grade modified trypsin (Promega) in a 50:1 ratio and kept at 37 °C overnight. Tryptic digests were acidified with 10% trifluoroacetic acid (TFA; Sigma) to pH 2–3, desalted with a C18 column (Agilent) and eluted with 80% acetonitrile (Sigma). Peptides were dried with a SpeedVac and resuspended in 0.05% TFA before mass spectrometry (MS) analysis.

2.10. Tandem mass spectrometry

Tandem mass spectroscopy (MS/MS) and data analysis were performed by the TRI Proteomics core facility. Purified peptides of 1 μg were loaded onto a C18, 20 MM × 75 μm ID column (THC164705 column) and separated with a C18, 500 MM × 50 μm ID easy column (THCES803) over 180 min on a Thermo Scientific Easy nLC 1000. The peptides were analyzed on a Q Exactive Plus orbitrap mass spectrometer and full MS spectra were acquired with a 70 k resolution, 3e6 AGC, and a maximum injection time of 100 ms. Top 10 precursors were selected for fragmentation at 27 NCE and MS/MS analysis. MS/MS spectra were acquired with 17.5 k resolution, 5e5 AGC, 50 ms max IT. Analyzed precursors were prevented from analysis for 30 s. The MS/MS data were processed with Sequest HT on Proteome Discoverer 2.3 and searched against the Swiss-Prot—human species protein database with the following settings: trypsin enzyme with a maximum of two miscleavages, fix carbamidomethylated cystine, variable oxidized methionine modifications, precursor and product mass tolerance ± 10 ppm and 0.02 Da, respectively. False discovery rate analysis was performed with Percolator, 1% FDR Strict and 5% FDR Relaxed. Protein summary included only valid proteins with less than 5% FDR. The data were normalized to total peptide and scaled to all average.

2.11. Functional annotation analysis

Functional annotation of differentially expressed proteins in CAFs and NPFs was conducted using the database for annotation, visualization, and integrated discovery (DAVID) [48,49]. Proteins with a fold change (FC) of ≥1.75 between CAF and NPF samples were considered differentially expressed. Overrepresented functional categories among the proteins were relative to whole genome background. The following categories were used for functional annotation and functional clustering: GeneOntology (GO) terms for the three subsets cellular component, molecular function, and biological process [50,51] as well as the Uniprot [52] and the KEGG pathway database [53]. The threshold for the EASE score, a modified Fisher's exact P-value was set to 0.1. A Z-score, defined as $(up - down)/(\sqrt{count})$, was calculated using R version 3.6.3 [54] and the package GOplot [55]. Up and down are the numbers of upregulated (logFC>0) and downregulated (logFC<0) proteins, and count represents the total count.

2.12. Orientation analysis

The OrientationJ plugin [56] in Fiji [57] (ImageJ 1.52p) was used for orientation distribution analysis. Briefly, maximum projections of the z-stacks were obtained. A representation of the angles of the F-actin fibers were characterized by hue-saturation-brightness color-coded images, where the different colors related to different absolute angles of

orientation. The distribution of orientation angles was assessed by analyzing the orientation and isotropic properties of individual pixels that together made up the fibers. A cubic spline gradient interpolation with a Gaussian window of $\sigma = 2$ for F-actin fibers was applied, which gave quantitative data for the distribution and frequency of angles from $-90°$ to $90°$. To enable comparison of various samples, peaks were normalized by rotating each angle by an alignment angle ϕ determined by the mode of the absolute angles. That way, for each images the principal axis was located parallel to the horizontal axis.

2.13. Shape analysis

The shape and the orientation of BPH-1 cells grown on fibroblasts was analyzed using the Shape Descriptors in Fiji [57] (ImageJ 1.52p). Segmentation of BPH-1 cells in 2D was achieved using the SCF H_Watershed plugin (MPI-CBG Dresden) [58] on maximum intensity projections of the z-stack image. Roundness $(4A)/(\pi l_{MA}^2)$ and elongation $(1 - S/L)$ were determined, where A is the area of the object, l_{MA} the length of the major axis of a fitted ellipse, S is the short, and L the long side of the minimum bounding rectangle of the object. Segmentation in 3D was achieved using the MorpholLib plugin [59]. The 3D objects counter plugin [60] was used to determine the surface area (A) and the volume (V) of the object and the sphericity was calculated by $\sqrt[3]{\pi}\sqrt[3]{\pi(6V)^2}/A$.

2.14. Peak distance analysis

Regions of interest (ROIs) were determined on maximum intensity projections of the GFP channel for each image. Using Fiji [57] (ImageJ 1.52p), a threshold was applied to the maximum intensity projection (Autothreshold, method 'Default') and dilation was used to include the neighboring area into the ROIs. Next, the ROIs were overlaid on the z-stack images and the mean grey intensity of each channel along the z-stack was measured. Under the assumption that, on a z-scale, objects have the highest intensity in the plane where they are localized, the GFP signal (representing BPH-1 cells) and the FN signal (representing the fibroblast matrix) were analyzed over the depth of the confocal image to estimate the penetration of BPH-1 cells into the fibroblast layer. The distance to FN matrix is defined by the distance between the GFP and the FN intensity peak over the z stack. Thus, a lower peak difference correlates with an increased level of invasion/infiltration.

2.15. Ki67 analysis

For Ki67 analysis, maximum intensity projections of z-stack images were used. The nuclei of GFP-positive cells with and without Ki67 staining present were counted using Fiji [57] (ImageJ 1.51w) and the cell counter plugin. The images were blinded during counting. The proliferative index is determined by the proportion of Ki67 high cells.

2.16. Statistical analysis

All data and statistical analysis was performed in R version 3.6.3 [54] with the following packages attached: ggplot2, ggpubr, tidyverse [61], scales, RDAVIDWebService [62], GOplot [55], and lme4 [63]. All data sets were tested for normal distribution using the Shapiro test. Normal distribution was assumed with p-values ≥ 0.05. For non-normally distributed and ranked data sets (orientation angle distributions; AFM and RT-FDC measurements on one patient) a Mann–Whitney U test was applied to determine statistical significance. Statistical significance in normally distributed data sets (peak difference, Ki67 counts) was tested using an unpaired student's t-test. To determine the correlation coefficient for alignment patterns, a Kendall tau test was performed. To analyze AFM data sets, R and lme4 [63] were used to perform a linear mixed effects analysis of the relationship between stiffness and fibroblast type. As fixed effects, we used fibroblast type (CAFs/NPFs), as random

effects we had intercepts for patients. Similarly, a linear mixed model analysis was performed for RT-FDC data in the ShapeOut software [64]. P-values in graphs as indicated as ***$p \leq 0.001$, **$p \leq 0.01$, *$p \leq 0.05$. Statistical significance was assumed with $p \leq 0.05$.

3. Results

3.1. Patient-matched cancer-associated fibroblasts and non-malignant prostate tissue fibroblasts have distinct cytoskeleton and extracellular matrix arrangements

To study the changes in the cell mechanics of tumor stroma, we established matrix-rich cultures of patient-matched prostatic fibroblasts. Primary fibroblasts were obtained from radical prostatectomy specimens of two patients with intermediate (grade group 2, patient 2) or high grade (grade group 5, patient 1) PCa (Supplementary Table S2). CAFs were isolated from confirmed malignant areas of tissue. Matched NPFs were isolated from contralateral regions of non-cancerous tissue from each prostate. A board-certified pathologist confirmed that the specimens of patient tissue that were used to establish the fibroblast cultures were benign (for NPFs) and malignant (for CAFs) (Fig. 1A and B) [36]. CAFs and NPFs from both patient-matched pairs exhibit distinct epigenome profiles [41] and show functional differences *in vitro* [17]. The fibroblasts were grown to confluency and induced for matrix secretion with ascorbic acid for 5 days. Firstly, we characterized the protein content of CAFs and NPFs from patient 1 using semiquantitative mass-spec analysis. Using a FC of 1.75, there were 1095 differentially expressed proteins between the CAF and NPF (Supplementary Table S3). Functional annotation of these proteins revealed increased levels of proteins involved in ECM components and organization as well as cell–substrate and cell–cell adhesion in CAFs compared with NPFs (Fig. 2A, Supplementary Fig. S1). To visualize both cell and ECM components, fibroblast cultures were stained for F-actin and FN, a highly abundant ECM protein in CAF matrices [18] (Fig. 2B and C, Supplementary Figs. S2A–B; left column of each panel). FN fibers, which were color-coded by their respective angle of orientation, exhibited a predominant color in CAFs but not in NPFs (Fig. 2B and C, Supplementary Figs. S2A–B; right column of each panel) indicating differences in fibril alignment. These observations were quantified by analyzing the orientation angles of individual FN fibers. Indeed, a narrow distribution with a distinct peak was found for CAF monocultures compared with NPFs, indicating a higher degree of parallel fibril alignment in CAFs (Supplementary Fig. S2D). Similarly, F-actin fibers were also more consistently aligned in CAFs vs. NPFs in both patients (Fig. 2E, Supplementary Fig. S2E). Overlaying F-actin and FN channels indicated that the alignment of both fiber types followed similar patterns (Fig. 2D). To evaluate the degree of co-alignment of FN and F-actin, the angles for FN fibrils were plotted with respect to the principal axis for F-actin, which yielded highly similar distributions. In CAFs, there was a high correlation (R^2 0.79 patient 1, R^2 0.82 patient 2), but a lower correlation in NPFs (R^2 0.69 patient 1 and R^2 0.57 patient 2) (Fig. 2F, Supplementary Fig. S2F).

Taken together, F-actin and FN fibers in CAFs but not in NPFs were characterized by a parallel alignment. These differences in the organization of the ECM and the F-actin cytoskeleton organization led us to investigate the biomechanical properties of CAF and NPF cultures.

3.2. Cancer-associated fibroblast monocultures and single cells are stiffer than non-malignant prostate tissue fibroblasts

We compared the mechanical properties of CAF and NPF monocultures by two different methods, AFM indentation and the high-throughput technique, RT-FDC (Fig. 3A). While AFM indentation tests the elastic properties of intact CAF and NPF monocultures, RT-FDC probes the deformation of suspended cells within a microfluidic channel, i.e. after releasing the cells from the matrix (Fig. 3B). RT-FDC revealed that CAFs were less deformed than NPFs (Fig. 3C). At the
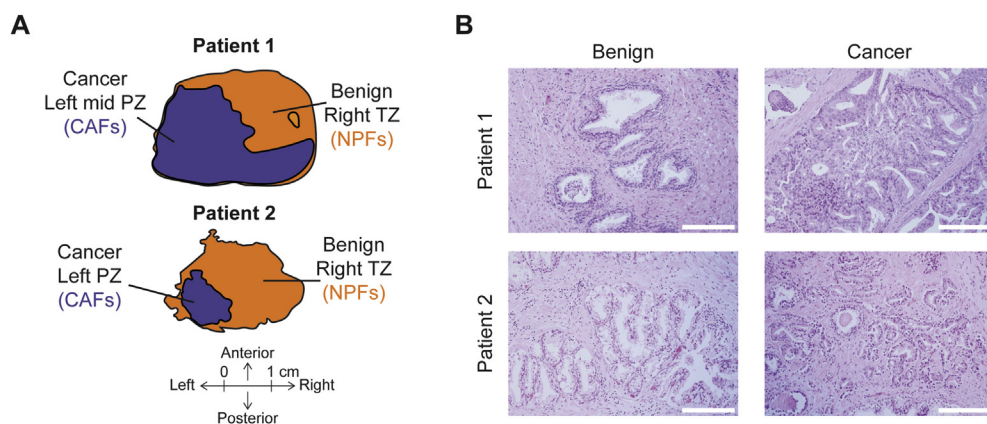
Fig. 1. Overview showing the isolation of cancer-associated fibroblasts (CAFs) and non-malignant prostate tissue fibroblasts (NPFs) from human prostate tissue (A) Pathology maps showing the location of index tumors (purple) within each patient's radical prostatectomy specimen (orange). The approximate location that each cancer and benign sample was dissected from is shown. (B) Representative images of hematoxylin and eosin staining showing the benign and cancer tissues from which cultures of NPFs and CAFs were established. Scale bar, 100 μm.

same time, the detected area for CAFs was significantly larger than for NPFs, indicating that CAFs had an increased cell size. Since larger cells are exposed to higher shear stresses in the channel, this indicates an increased cell stiffness for CAFs, which was confirmed by calculation of apparent Young's moduli. The apparent elastic moduli were significantly higher for CAFs (median: 1.1 kPa) than for NPFs (median: 0.9 kPa; Fig. 3D and E, Supplementary Table S4), corresponding to a 20% increase. In line with these results, AFM indentation tests revealed an increase in the apparent Young's modulus of CAFs (median: 1.9 kPa patient 1; 2.5 kPa patient 2) compared with NPFs (median: 1.1 kPa patient 1; 1.6 kPa patient 2). The differences in median apparent Young's moduli were more extensive (75% in patient 1; Fig. 3F, and 62% in patient 2; Supplementary Fig. S2G, Supplementary Table S4) when intact cell layers were probed by AFM. Furthermore, apparent elastic moduli of patient 1 were generally lower than in patient 2 (change of median between patients: 30% for NPFs, 25% for CAFs).

In summary, these results indicate that CAFs were significantly stiffer compared with NPFs, not only when probed spread in culture with the surrounding matrix but also after their release.

3.3. In co-cultures, cancer-associated fibroblasts induce morphological changes in benign epithelial prostate cells

Following the assessment of the fibroblast characteristics, we studied epithelial–stromal interactions by co-culturing BPH-1 cells together with pre-formed CAF and NPF cultures for 48 h. The distinct alignment of FN fibers and the F-actin cytoskeleton between CAFs and NPFs was maintained in the presence of epithelial cells (Supplementary Figs. S3A–F). However, differences in the morphology of BPH-1 cells in co-culture with fibroblasts were observed (Fig. 4A). On NPFs, BPH-1 cells were round and formed clusters (Fig. 4A, left column of each panel). In contrast, in co-culture with CAFs, BPH-1 cells were elongated and aligned with the fibroblast cells (Fig. 4A, right column of each panel). BPH-1 grown on plain tissue culture plastic displayed a cobblestone-like morphology (Fig. 4A, far right panel). Morphometric analysis confirmed the qualitative observations. BPH-1 grown in the presence of CAFs were more elongated (Fig. 4B, center panel). In contrast, on NPFs, the epithelial cells displayed a more circular (Fig. 4B, left panel) and spherical shape (Fig. 4B, right panel) in 2D and 3D, respectively. The morphological phenotype of BPH-1 cells co-cultured with NPFs was similar to the cells cultivated on plain tissue culture plastic surfaces (Fig. 4A and B). These morphological changes are consistent with previously reported observations [17,37] (Supplemental Table S2). The relationship between the fibroblast and BPH-1 cell orientation was further investigated by comparing their respective angles of orientation. The highly similar angle distribution indicated that BPH-1 cells extended along the CAFs (R^2 0.65, patient 1, and 0.72, patient 2; Fig. 4C). Similar results were found for the relationship between epithelial cell and FN fiber alignment in CAFs (R^2

0.76, patient 1, and 0.71, patient 2; Fig. 4D). For NPFs, the correlation coefficients (R^2 -0.42 for F-actin, R^2 0.46 for FN, patient 1, and R^2 0.32 for F-actin, R^2 0.45 for FN, patient 2) were found to be lower indicating a weaker correlation.

The morphological changes indicate that BPH-1 cells remodeled their cytoskeleton in co-cultures. To determine whether the co-culture of BPH-1 cells with fibroblasts also affected the mechanical properties of BPH-1, NPFs, and CAFs, we next measured their elastic properties.

3.4. Benign prostate epithelial-1 cells acquire a more compliant mechanical phenotype on co-culture with cancer-associated fibroblasts, while cancer-associated fibroblasts remain stiffer than non-malignant prostate tissue fibroblasts

We isolated fibroblasts and BPH-1 cells from the co-cultures and probed their mechanical properties (Fig. 5A). Epithelial and stromal cells were distinguished based on the green fluorescence emission of the GFP-positive BPH-1 cells and GFP-negative fibroblasts. In RT-FDC measurements, the two discrete cell populations were separated by gating for the GFP-positive fraction [47] (Fig. 5B), while in AFM indentation tests cells were distinguished by visual inspection. Both, AFM and RT-FDC indicated that CAFs retained their stiffer phenotype in co-culture with BPH-1 cells in both an attached state and after release from the matrix, respectively (Fig. 5C and D). Fibroblasts grown in the presence of BPH-1 were stiffer (AFM measured median elastic modulus of 3.3 kPa, NPFs and 3.95 kPa CAFs; RT-FDC measured median elastic modulus of 1.4 kPa NPFs and 1.97 kPa CAFs, all patient 1) than grown in monoculture (AFM measured median elastic modulus of 1.1 kPa NPFs and 1.9 kPa CAFs; RT-FDC measured median elastic modulus of 0.9 kPa NPFs and 1.05 kPa CAFs, all patient 1). This was consistent across NPFs and CAFs from both patients (Supplementary Table S4).

In contrast to fibroblasts, BPH-1 cells released from the co-cultures had significantly decreased apparent Young's moduli. Median apparent Young's moduli detected by AFM for BPH-1 after co-culture with CAFs were 0.97 kPa and 0.93 kPa for patient 1 and patient 2, respectively, and 1.29 kPa and 1.22 kPa for NPFs patient 1 and patient 2, respectively. The elastic modulus of BPH-1 on CAFs was decreased by approximately 25% compared with NPFs (Fig. 5E, Supplementary Table S4). The same trend was observed for RT-FDC measurements where the apparent elastic moduli were slightly higher with 2.2 kPa for BPH-1 on CAF for both patients, compared with 2.5 and 2.4 kPa for BPH-1 on NPF patient 1 and 2, respectively, corresponding to an approximately 10% decrease in stiffness on CAFs (Fig. 5F, Supplementary Table S4). Similar changes in the mechanical phenotype of BPH-1 cells were observed, when they were exposed to conditioned medium from fibroblasts instead of a direct co-culture (Supplementary Fig. S4A).

Thus, while CAFs were stiffer than NPFs, co-culture with CAFs induced a more compliant mechanical phenotype in BPH-1 cells. The
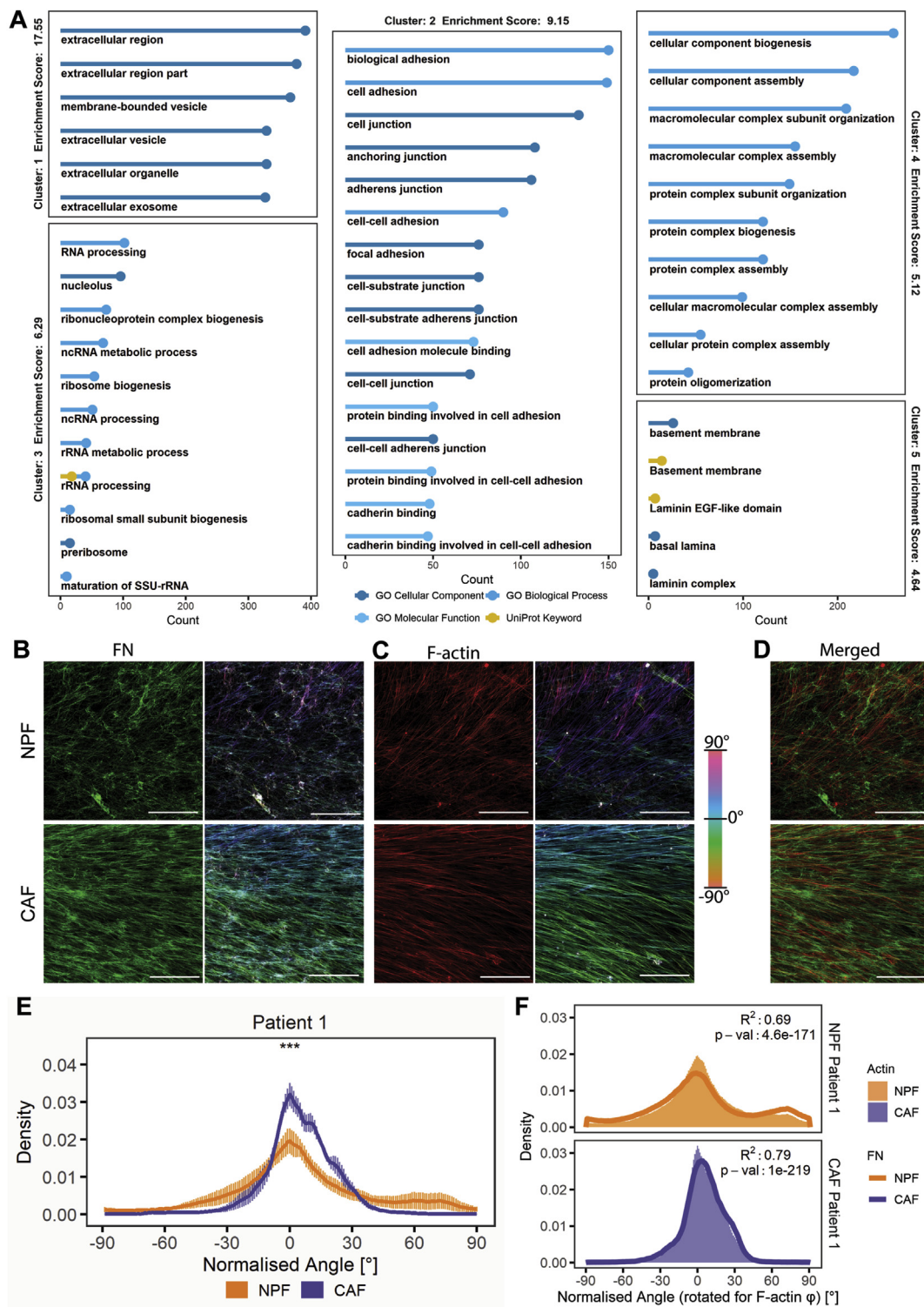
Fig. 2. Patient-matched cancer-associated fibroblasts (CAFs) and non-malignant prostate tissue fibroblasts (NPFs) have distinct cytoskeleton and extracellular matrix (ECM) arrangements. (A) Differential protein expression in CAFs vs. NPFs from patient 1. DAVID tool was used for functional annotation and clustering of differentially expressed proteins. Proteins involved in ECM organization, cell–cell adhesion, and cell–substrate interactions are highly expressed in CAFs (clusters 1, 2, 4, 5) while RNA processing–related proteins (cluster 3) are lower compared with NPFs. Compare also Fig. S1. (B/C) Representative maximum intensity projection images of immunofluorescence staining for FN and F-actin (left columns of each panel; green—FN, red—F-actin) of patient 1. The images were pseudo-color coded for the absolute orientation angle (left columns of each panel). (D) Merged images of FN (B) and F-actin staining (C). Scale bar 100 μm. (E) Quantitative analysis of F-actin orientation patterns in patient 1. Absolute angles are plotted relative to the principle axis. Graphs represent mean ± SEM (n = 4 images per group). (F) Orientation of FN is correlated with the alignment of F-actin filaments. For each image, the FN channel was rotated using the alignment angle ϕ for F-actin. The filled area shows the orientation distribution of actin filaments (rotated by ϕ for F-actin). The line graph represents the orientation distribution of FN (rotated by ϕ for F-actin). A correlation coefficient (R^2) is given for each sample (n = 4 images per group).
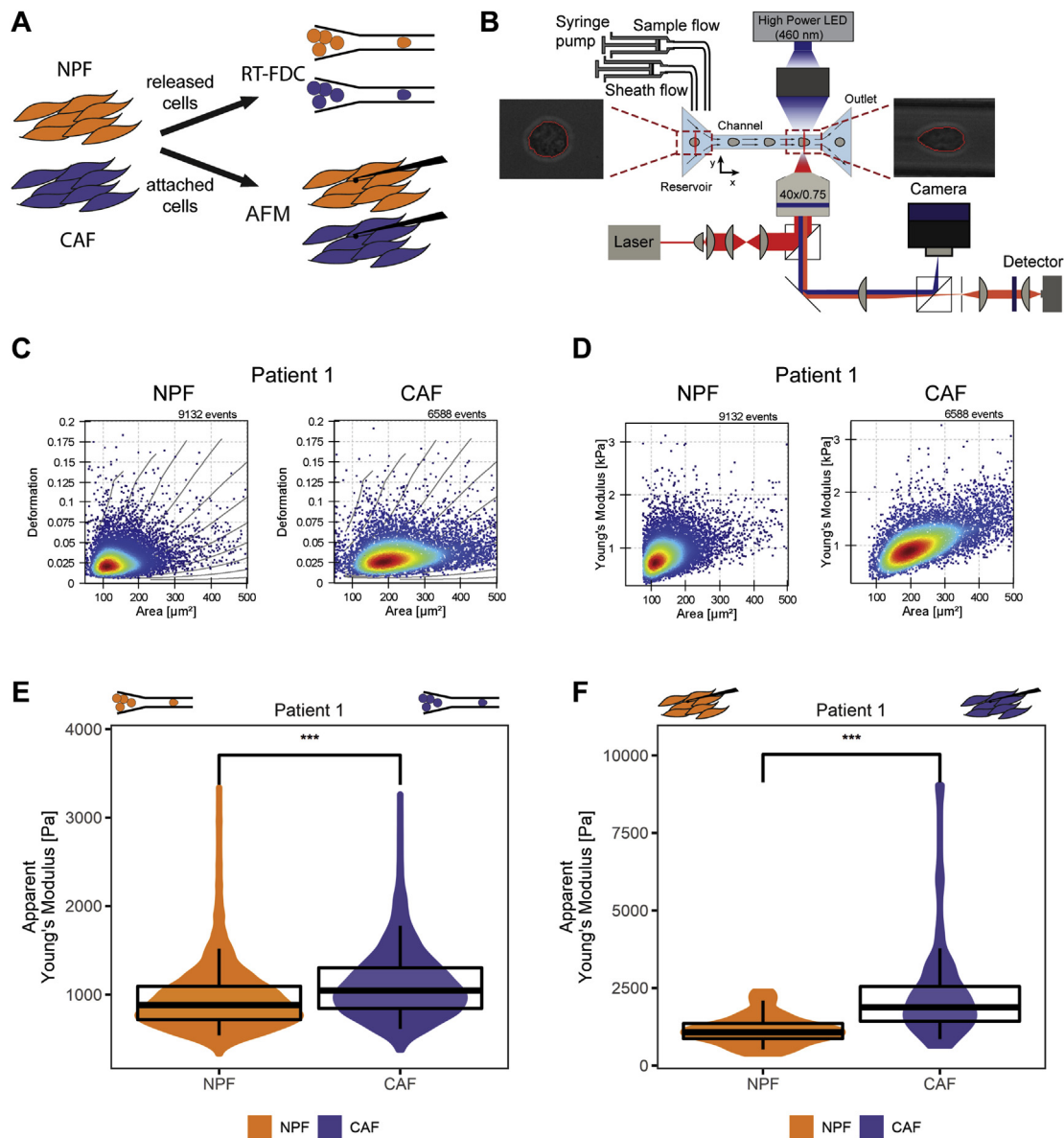
Fig. 3. Biomechanical characterization of CAFs and non-malignant prostate tissue fibroblasts (NPFs). (A) Schematic representation of the biomechanical characterization. (B) Real-time deformability cytometry (RT-FDC) setup. Sample and sheath flow are combined and flushed through a microfluidic channel. Before entering the channel, cells pass through a reservoir where they exhibit an undeformed round shape (left hand side photo). On entering the narrow, 30 µm wide microfluidic channel, the cells are deformed (right hand side photo). The software acquires the image and detects the outline on the fly (indicated in red in photo). The deformation is defined as 1-circularity and calculated in real time. (C/D) Scatterplots of deformation (C) and apparent Young's modulus (D) vs. area of CAFs (right) and NPFs (left). (E/F) Cells were probed after release using RT-FDC (E) and as intact cultures using AFM (F). Quantitative representation of the data as violin plots and boxplots. Box representing the median and 25/75 percentile, whiskers represent 5/95 percentile (RT-FDC n ≥ 6470 cells per group; AFM n ≥ 45 cells per group). The median apparent elastic moduli are listed in Supplementary Table S4.

decreased stiffness of suspended BPH-1 cells on co-culture with CAFs likely reflects changes in the cytoskeleton of BPH-1 cells, in particular, of the cell cortex. Additionally, BPH-1 cells were analyzed while being attached to the fibroblast cultures using AFM. However, it turned out more difficult to probe BPH-1 cells in co-cultures, since a large proportion of cells were interspersed within the CAF layer. Nevertheless, the epithelial cells were also more compliant on CAFs, a similar trend as for the released cells (Supplementary Fig. S4B).

3.5. Benign epithelial cells are more invasive and proliferative in co-culture with cancer-associated fibroblasts

To evaluate BPH-1 cell infiltration into the CAF cultures, we determined the localization of epithelial cells within the fibroblast matrix by

analyzing z-stack images of the co-cultures stained for FN. After overnight co-culture, orthogonal sections showed that BPH-1 cells were mostly located on top of the FN layer. However, after 48 h of co-culture, most BPH-1 cells had moved into the CAF matrix, but not the NPF matrix (Fig. 6A). Quantitative analysis confirmed that BPH-1 cells penetrated deeper into the FN matrix produced by CAFs compared with NPFs (both patient pairs) as indicated by a smaller peak difference (see Methods and Supplementary Fig. S4C). However, differences in absolute migration depth and variability between patient pairs were found (Fig. 6B).

The proliferation of BPH-1 cells in co-culture with CAFs or NPFs was compared by Ki67 staining. An increased amount of Ki67 positive BPH-1 cells was found on co-culture with CAFs (37% patient 1, 64% patient 2) compared with NPFs (19% patient 1, 43% patient 2; Fig. 6C). Interestingly, co-culture with either fibroblast type was found to be growth

inhibitory compared with tissue culture plastic where 70% of BPH-1 were Ki67 positive (Fig. 6C). Additionally, we confirmed the increased proliferation of BPH-1 cells in the presence of CAFs using the GFP signal (Supplementary Fig. S4D).

In summary, our results show that CAF and NPF cultures display distinct arrangements of ECM and F-actin cytoskeleton, which correlates with increased cellular stiffness of CAFs. Moreover, CAFs induced morphological changes in BPH-1 cells, accompanied by a decreased
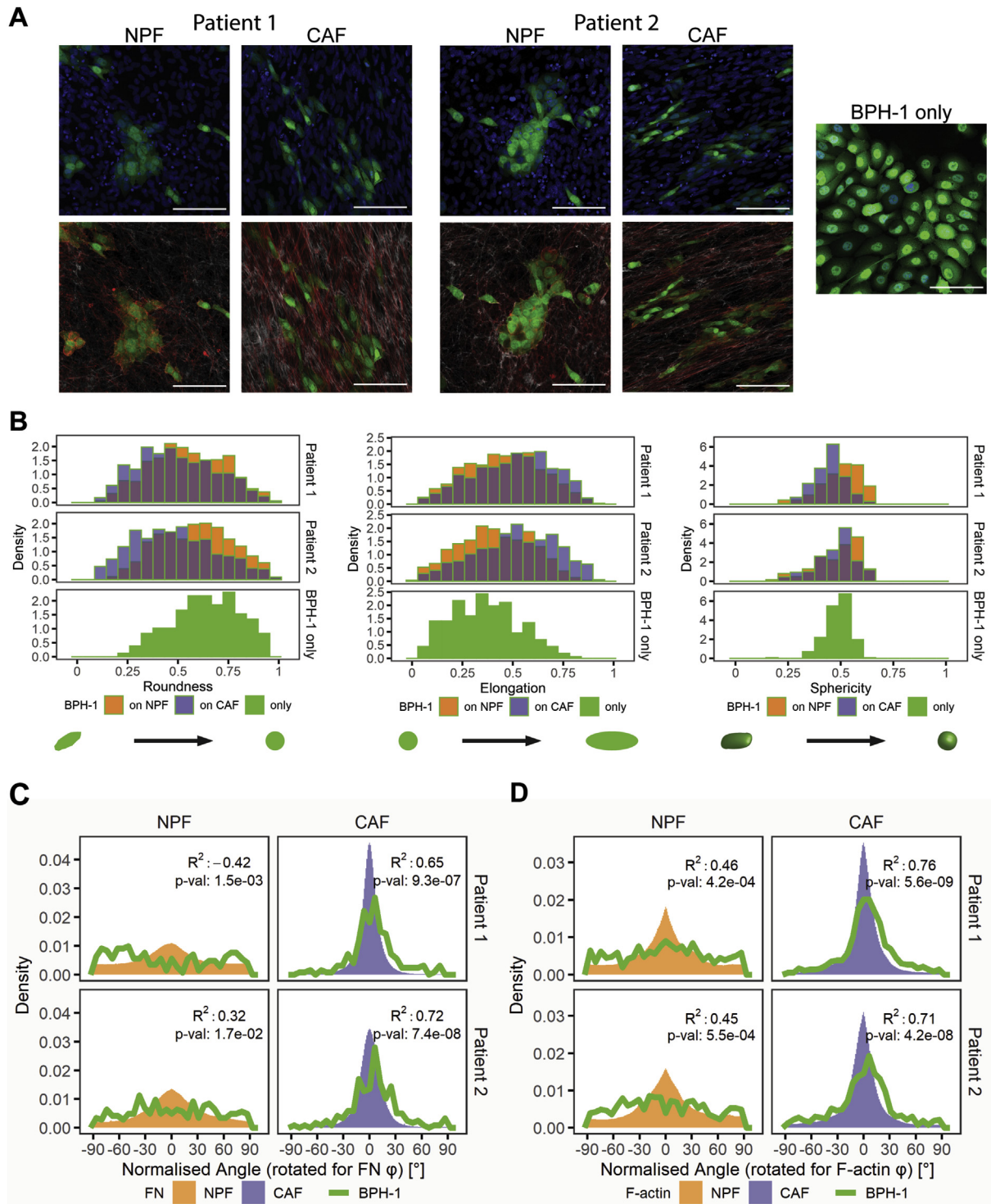

Fig. 4. Morphological features and elastic properties of BPH-1 in co-culture with non-malignant prostate tissue fibroblasts (NPFs) and cancer-associated fibroblasts (CAFs). (A) Representative maximum intensity projections of immunofluorescence staining show epithelial cell morphology. Blue—DAPI, green—GFP (BPH-1), red—FN, and grey—F-actin. Scale bar 100 μm. (B) Characterization of BPH-1 shapes on NPFs and CAFs using shape descriptors (roundness and elongation in 2D and sphericity in 3D) (n = 6 images BPH-1 monocultures, n ≥ 12 images per group co-cultures). (C/D) BPH-1 orientation along FN fibers (C) and actin filaments (D). The filled area shows the orientation distribution of FN fibers (rotated by ϕ for FN; C) or actin filaments (rotated by ϕ for F-actin; D). The line graph represents the orientation distribution of the BPH-1 cells (rotated by ϕ for FN (C) or F-actin (D). A correlation coefficient (R^2) is given for each sample (ROI from n ≥ 6 images per group).
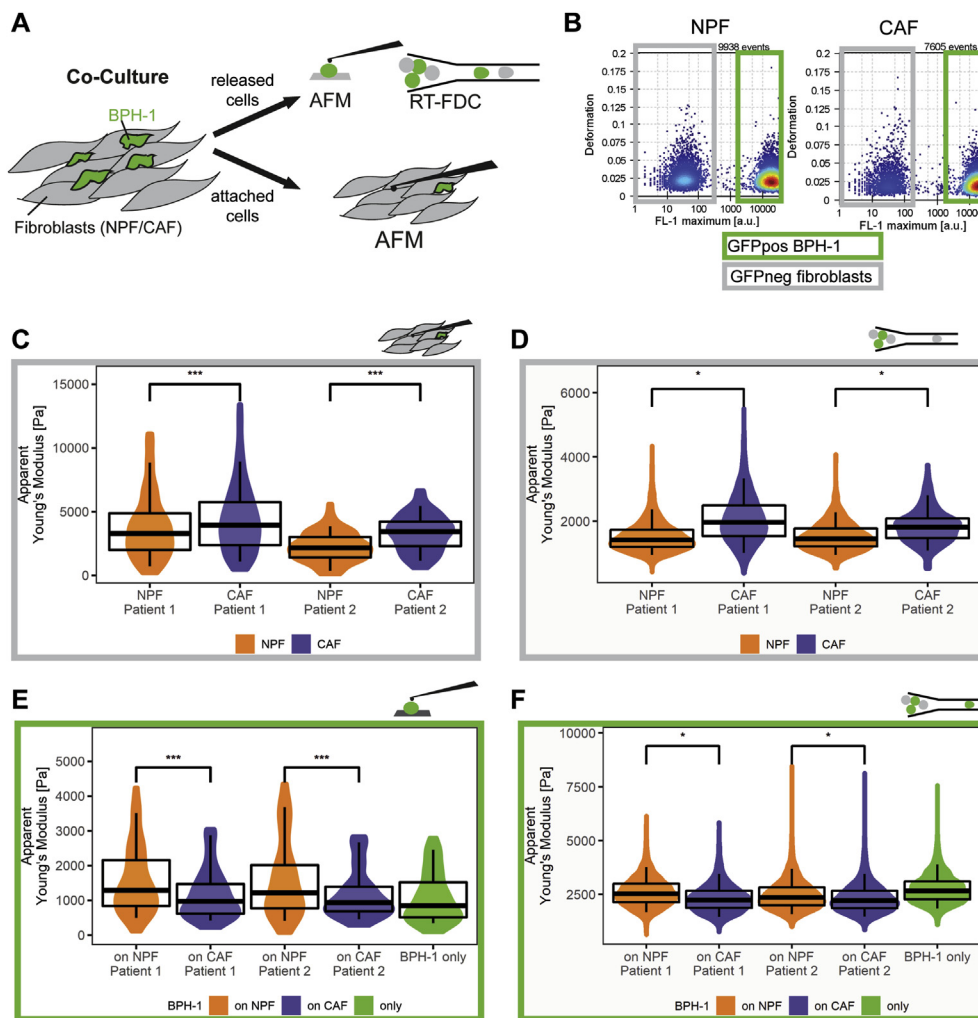
Fig. 5. BPH-1 cells adopt a more compliant mechanical phenotype on co-culture with cancer-associated fibroblasts (CAFs) while CAFs remain stiffer than non-malignant prostate tissue fibroblasts (NPFs). (A) Schematic representation of elastic measurements of fibroblasts and epithelial cells in co-culture. (B) GFP signal was used to distinguish between both cell types in co-culture. Scatterplot of the RT-FDC measurement representing fluorescence on the x axis and deformation on the y axis, representative for patient 1. (C/D) CAFs remain stiffer than NPFs in a co-culture with BPH-1 while being attached to the matrix (atomic force microscopy [AFM]; C) as well as in suspension (RT-FDC; D). (E/F) BPH-1 cells have a lower elastic modulus after cultured in the presence of CAFs determined by AFM (E) and RT-FDC (F). Elastic modulus data are represented as violin and boxplots. Boxplot boxes are representing the median and 25/75 percentile, whiskers represent 5/95 percentile (AFM, fibroblasts on matrix n ≥ 99 cells per group, RT-FDC, released fibroblasts n ≥ 376 cells per group, AFM released BPH-1 n ≥ 60 cells per group, RT-FDC released BPH-1 n ≥ 2690 cells per group). The median apparent elastic moduli are listed in Supplementary Table S4.

apparent Young's modulus and increased invasiveness and proliferation compared with BPH-1 cells co-cultured with NPFs.

4. Discussion

In this work, we demonstrated that CAFs exhibit a highly aligned F-actin cytoskeleton and ECM and are stiffer compared with patient-matched NPFs. MS analysis revealed upregulation of proteins involved in ECM deposition, cell–cell and cell–substrate adhesion in patient 1. These findings are in line with differential protein expression recently reported for patient 2 and other patient-matched pairs of prostate fibroblasts [38]. Here we found distinct differences in ECM architecture between CAFs and NPFs, with more elongated and uniformly oriented FN fibrils for CAFs, similar to previous reports [16–19,38,65]. A distinct pattern of collagen fibril orientation was previously found *in situ* using second harmonic imaging in malignant foci of PCa biopsy samples [66].

We observed an increased apparent Young's modulus in CAFs compared with their patient-matched NPFs both as spread (measured by AFM) and suspended (by RT-FDC) cells. The absolute values of apparent Young's moduli detected by both methods, however, are not directly comparable as they are influenced by the cellular states (attached vs. suspended) and intrinsic differences of the measurement techniques, which operate at different time scales (seconds range in AFM, milliseconds in RT-FDC). The increased apparent Young's moduli of attached CAF cultures probed by AFM likely reflect changes in mechanical properties of both the fibroblasts and their surrounding ECM. A previous report noted that CAF-derived decellularized matrices are stiffer compared with

normal fibroblast matrices in head and neck squamous cell carcinoma [19]. Increased matrix stiffness is a well-described feature of solid tumors [67] and the adjacent stromal tissue [68]. In turn, changes in stiffness and structural arrangements of the ECM are expected to modulate the F-actin cytoskeleton providing mechanical feedback [69,70]. The increased elastic moduli of released CAFs measured by RT-FDC, where no intact ECM bundles were present, confirms that CAFs themselves are stiffer than NPFs. Both local AFM indentation tests and whole-cell indentation tests, such as by RT-FDC, are dominated by the mechanical properties of the actomyosin cortex of the cells [71]. It is expected though that the mechanical properties of the cell cortex in a spread and a suspended state vary, as the cortical thickness depends on cell spreading and is altered on de-adhesion of cells [72]. Recently, pancreatic CAFs were reported to exhibit a lowered elastic modulus compared with native fibroblasts from the pancreas, although similar changes in the stress fiber alignment as in our study were observed [73,74]. There are, however, some differences in the experimental setup. We used dense ECM-enriched cultures from patient-matched prostate fibroblasts and probed them with a small spherical indenter. In contrast, Sylianou et al. [73,74] probed non-confluent pancreatic fibroblasts that were immortalized. While organ-specific differences might not be excluded, we also detected patient-to-patient variability in our experiments. This underlines the importance of using patient-matched pairs to study normal and CAFs.

Besides the increased cell stiffness, we found that CAFs were larger than NPFs. There could be various reasons for size alterations. For instance, a different cell cycle progression can cause differences in average cell size [75]. However, we excluded in this case, since the
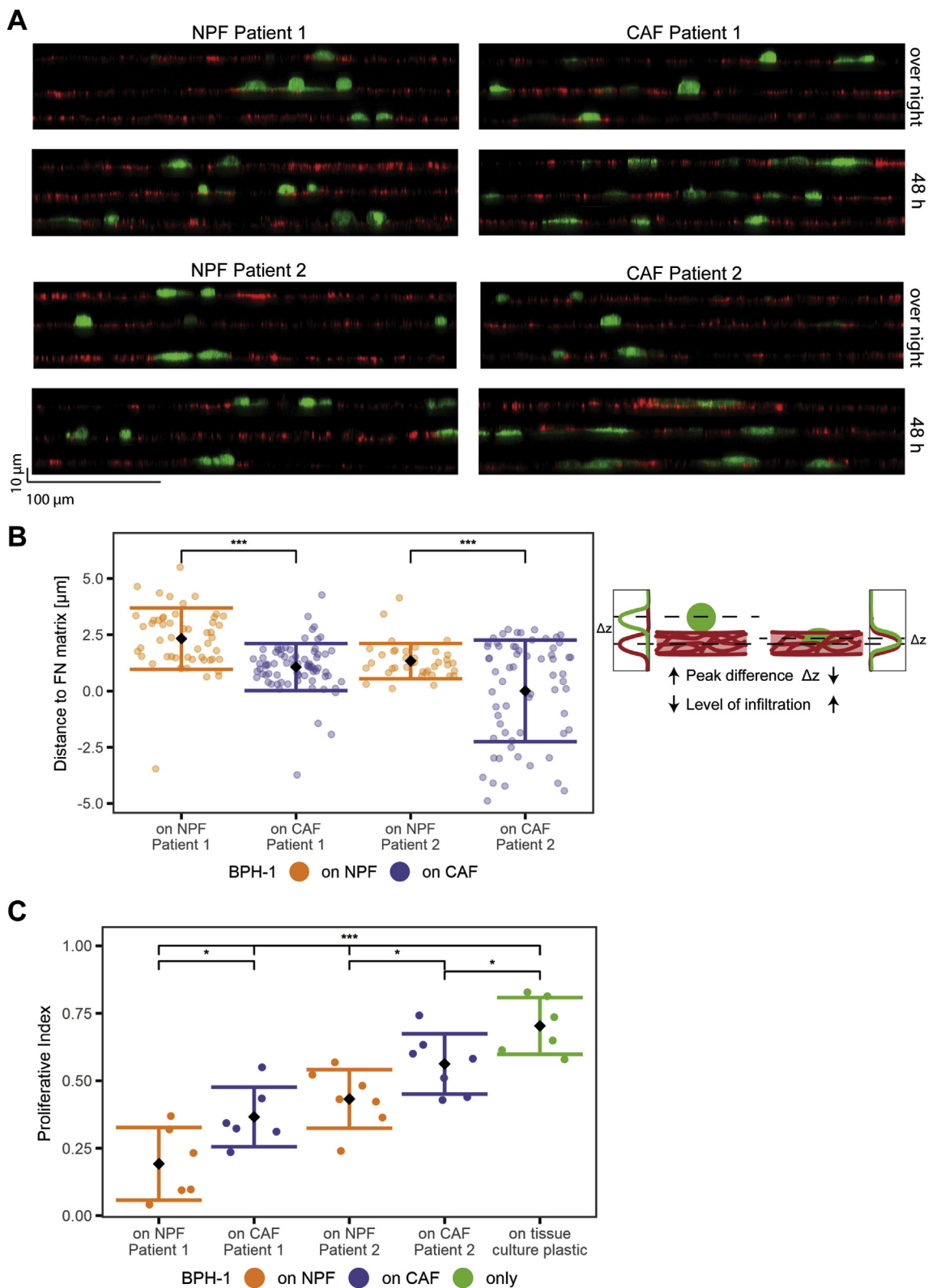
Fig. 6. BPH-1 are more invasive and proliferative in the presence of cancer-associated fibroblasts (CAFs). (A) Representative orthogonal projections of immuno-fluorescence staining (green—GFP [BPH-1], red—FN) of BPH in co-culture with CAFs or non-malignant prostate tissue fibroblasts (NPFs) overnight and after 48 h. (B) Distance between BPH-1 cells and FN matrix. Data are represented as mean (black diamond) ± standard deviation. Single points represent regions of interest (ROIs); (ROIs from n ≥ 6 images per group). (C) Proliferation of BPH-1 cells in the presence of CAFs or NPFs determined by Ki67 staining. Data represented as mean (black diamond) ± standard deviation. Single points represent analyzed images (counts of n ≥ 6 images per group).

analyzed fibroblasts were highly confluent and showed a very low proliferative activity (data not shown). Moreover, the hippo pathway has been associated with cell size control [76]. Its key effector YAP/TAZ is associated with increased cellular tension [77,78] and has been linked to ECM remodeling and stiffening by mammary CAFs [65]. RhoA-ROCK inhibition in CAFs prevented cell size changes as well as the formation of stress fibers, suggesting a role of RhoA-ROCK signaling [79]. In our study, we stained for YAP/TAZ (data not shown), but as we found YAP/TAZ localization to be highly dependent on confluency, it was not feasible to draw conclusions from this data. Further studies are needed to investigate the cause of the cell size differences in CAFs and NPFs.

While CAFs were found to be stiffer compared with patient-matched NPFs, BPH-1 cells became more compliant when co-cultured together with CAFs compared with NPFs. The biomechanical alterations coincided with a more elongated spreading morphology with less prominent cell–cell contacts of BPH-1 in the presence of CAFs compared with monocultures and co-cultures with NPFs. The morphological phenotype is consistent with previous reports on benign epithelial cells and fibroblasts from the prostate [17,37]. Both the morphological changes and the observed lowered cell elastic modulus have been recently linked to a more migrative, invasive and malignant phenotype [17,29–31,37,80]. Cancer cell migration through dense ECM arrangements requires cellular deformability for which a more compliant phenotype can provide an advantage [81,82]. In line with this, we observed that the more compliant BPH-1 cells infiltrated deeper into the fibroblast layer. In PC3 cells, epithelial-to-mesenchymal transition (EMT) can be induced by prostatic CAFs through paracrine signals [15]. Also, the elongated morphology [67, 83] and the more compliant mechanical phenotype [83–85] point toward EMT. Staining for vimentin and panCK in BPH-1 cells grown in the presence of NPFs or CAFs did not reveal any significant differences (data not shown). The co-culture period of 48 h might show rapid morphological changes rather than full phenotypic transitions, and further studies are needed to investigate the molecular signature of the compliant BPH-1 cells. In our co-cultures, the benign epithelial cells were likely sensitive to the mechanical properties of the fibroblast-derived matrix as well as the stiffness of the fibroblasts themselves. Cells respond to their mechanoenvironment by adapting their cytoskeletal and mechanical properties when exposed to mechanical cues [86,87], although opposed responses have been reported. For instance, PCa (PC-3) cells reduced their cellular elastic modulus in response to an increased substrate stiffness [88], while fibroblasts stiffened [89]. The adaptive response of cancer cell lines to substrate stiffness might also be related to their invasive properties as previously suggested [80]. In contrast to the aforementioned studies conducted on gels of different stiffness, in our co-cultures, epithelial cells are not only exposed to different matrix stiffness but also a different matrix architecture and factors secreted by the fibroblasts [13]. Indeed, we observe comparable changes in biomechanical properties in BPH-1 cells with fibroblast conditioned medium. A similar effect of lowering cell stiffness was recently reported for mammary epithelial cells treated with TGF-β [83,90]. *In situ*, stromal and epithelial cells interact through a variety of biochemical and biomechanical signals as well as cell–cell contacts, which play essential roles in malignant transformation [3–5]. Similarly, in our experimental system, a concerted effect of soluble factors, direct cell–cell contacts, the altered mechanical environment, and ECM assembly might have been responsible for the alterations in morphology, mechanical properties, and proliferative and migratory response.

While consistent changes in mechanics, proliferation and morphology were found across the two donor pairs used within this study, this data set does not allow to correlate clinical parameters and mechanical phenotype, for which experiments across a larger panel of PCa samples should be conducted in the future.

5. Conclusion

Here we show that tumor-associated fibroblast cultures from the prostate are stiffer compared with NPFs. On co-culture with CAFs, BPH-1 cells exhibited a more elongated morphology and a more compliant mechanical phenotype, correlating with increased invasion and proliferation. In conjunction with the cellular phenotype and the gene expression profile [91,92], the mechanical properties of the reactive stroma could potentially be used for mechanical phenotyping of CAFs and new diagnostic approaches.

Author contributions

Anna Jaeschke: Investigation, Methodology, Data curation, Formal analysis, Visualisation, Writing - Original draft; **Angela Jacobi:** Investigation, Methodology, Data curation, Formal analysis, Visualisation, Writing - review and editing; **Mitchell Lawrence:** Investigation, Methodology, Visualisation, Resources, Writing - review and editing; **Gail Risbridger:** Supervision, Resources, Writing - review and editing; **Mark Frydenberg:** Investigation, Methodology, Writing - review and editing; **Elizabeth Williams:** Supervision, Writing - review and editing; **Ian Vela:** Supervision, Writing - review and editing; **Dietmar Hutmacher:** Supervision, Resources, Writing - review and editing; **Laura Bray:** Funding acquisition, Investigation, Conceptualisation, Resources, Supervision, Writing - reviewing and editing; **Anna Taubenberger:** Conceptualisation, Investigation, Methodology, Resources, Writing - reviewing and editing;

Declaration of competing interest

The authors declare that they have no known competing financial interests or personal relationships that could have appeared to influence the work reported in this paper.

Appendix A. Supplementary data

Supplementary data to this article can be found online at https://doi.org/10.1016/j.mtbio.2020.100073.

References

[1] J. Ferlay, M. Ervin, M. Colombet, L. Mery, M. Piñeros, A. Znaor, I. Soerjomataram, F. Bray, Cancer Today, Global Cancer Observatory: Cancer Today, International Agency for Research on Cancer, Lyon, France, 2018. http://gco.iarc.fr/today/home. (Accessed 23 April 2020).

[2] N. Howlader, A. Noone, M. Krapcho, D. Miller, A. Brest, M. Yu, J. Ruhl, Z. Tatalovich, A. Mariotto, D. Lewis, H. Chen, E. Feuer, K. Cronin, SEER Cancer Statistics Review, 1975. https://seer.cancer.gov/csr/1975_2016/.

[3] R.A. Taylor, G.P. Risbridger, Prostatic tumor stroma: a key player in cancer progression, Curr. Cancer Drug Targets 8 (2008) 490–497, https://doi.org/10.2174/156800908785699351.

[4] S.L. Shiao, G.C.-Y. Chu, L.W.K. Chung, Regulation of prostate cancer progression by the tumor microenvironment, Canc. Lett. 380 (2016) 340–348, https://doi.org/10.1016/j.canlet.2015.12.022.

[5] D.A. Barron, D.R. Rowley, The reactive stroma microenvironment and prostate cancer progression, Endocr. Relat. Canc. 19 (2012) R187–R204, https://doi.org/10.1530/erc-12-0085.

[6] D. Quail, J. Joyce, Microenvironmental regulation of tumor progression and metastasis, Nat. Med. 19 (2013) 1423–1437, https://doi.org/10.1038/nm.3394.

[7] A.F. Olumi, G.D. Grossfeld, S.W. Hayward, P.R. Carroll, T.D. Tlsty, G.R. Cunha, Carcinoma-associated fibroblasts direct tumor progression of initiated human prostatic epithelium, Canc. Res. 59 (1999) 5002–5011, https://doi.org/10.1186/bcr138.

[8] C. Frantz, K.M. Stewart, V.M. Weaver, The extracellular matrix at a glance, J. Cell Sci. 123 (2010) 4195–4200, https://doi.org/10.1242/jcs.023820.

[9] M. Ojalill, P. Rappu, E. Siljamäki, P. Taimen, P. Boström, J. Heino, The composition of prostate core matrisome in vivo and in vitro unveiled by mass spectrometric analysis, Prostate 78 (2018) 583–594, https://doi.org/10.1002/pros.23503.

[10] S.W. Hayward, M.A. Rosen, G.R. Cunha, Stromal-epithelial interactions in the normal and neoplastic prostate, Br. J. Urol. 79 (1997) 18–26, https://doi.org/10.1111/j.1464-410x.1997.tb16917.x.

[11] J.A. Tuxhorn, G.E. Ayala, D.R. Rowley, Reactive stroma in prostate cancer progression, J. Urol. 166 (2001) 2472–2483, https://doi.org/10.1016/s0022-5347(05)65620-0.

[12] J.A. Tuxhorn, G.E. Ayala, M.J. Smith, V.C. Smith, T.D. Dang, D.R. Rowley, Reactive stroma in human prostate cancer: induction of myofibroblast phenotype and extracellular matrix remodeling, Clin. Canc. Res. 8 (2002) 2912–2923.

[13] M. Ao, O.E. Franco, D. Park, D. Raman, K. Williams, S.W. Hayward, Cross-talk between paracrine-acting cytokine and chemokine pathways promotes malignancy in benign human prostatic epithelium, Canc. Res. 67 (2007) 4244–4253, https://doi.org/10.1158/0008-5472.can-06-3946.

[14] M.S. Joesting, S. Perrin, B. Elenbaas, S.E. Fawell, J.S. Rubin, O.E. Franco, S.W. Hayward, G.R. Cunha, P.C. Marker, Identification of SFRP1 as a candidate mediator of stromal-to-epithelial signaling in prostate cancer, Canc. Res. 65 (2005) 10423–10430, https://doi.org/10.1158/0008-5472.can-05-0824.

[15] E. Giannoni, F. Bianchini, L. Masieri, S. Serni, E. Torre, L. Calorini, P. Chiarugi, Reciprocal activation of prostate cancer cells and cancer-associated fibroblasts stimulates epithelial-mesenchymal transition and cancer stemness, Canc. Res. 70 (2010) 6945–6956, https://doi.org/10.1158/0008-5472.can-10-0785.

[16] P.P. Provenzano, K.W. Eliceiri, J.M. Campbell, D.R. Inman, J.G. White, P.J. Keely, Collagen reorganization at the tumor-stromal interface facilitates local invasion, BMC Med. 4 (2006) 38, https://doi.org/10.1186/1741-7015-4-38.

[17] B.A. Pereira, N.L. Lister, K. Hashimoto, L. Teng, M. Flandes-Iparraguirre, A. Eder, A. Sanchez-Herrero, B. Niranjan, M. Frydenberg, M.M. Papargiris, M.G. Lawrence, R.A. Taylor, D.W. Hutmacher, S.J. Ellem, G.P. Risbridger, E.M. De-Juan-Pardo, Tissue engineered human prostate microtissues reveal key role of mast cell-derived tryptase in potentiating cancer-associated fibroblast (CAF)-induced morphometric transition in vitro, Biomaterials 197 (2019) 72–85, https://doi.org/10.1016/j.biomaterials.2018.12.030.

[18] B. Erdogan, M. Ao, L.M. White, A.L. Means, B.M. Brewer, L. Yang, M.K. Washington, C. Shi, O.E. Franco, A.M. Weaver, S.W. Hayward, D. Li, D.J. Webb, Cancer-associated fibroblasts promote directional cancer cell migration by aligning fibronectin, J. Cell Biol. 216 (2017) 3799–3816, https://doi.org/10.1083/jcb.201704053.

[19] R. Raukonen, A. Mai, M. Georgiadou, M. Saari, N. De Franceschi, T. Betz, H. Sihto, S. Ventelä, L. Elo, E. Jokitalo, J. Westermarck, P.-L. Kellokumpu-Lehtinen, H. Joensuu, R. Grenman, J. Ivaska, Normal stroma suppresses cancer cell proliferation via mechanosensitive regulation of JMJD1a-mediated transcription, Nat. Commun. 7 (2016), https://doi.org/10.1038/ncomms12237.

[20] O. Chaudhuri, S.T. Koshy, C. Branco da Cunha, J.-W. Shin, C.S. Verbeke, K.H. Allison, D.J. Mooney, Extracellular matrix stiffness and composition jointly regulate the induction of malignant phenotypes in mammary epithelium, Nat. Mater. 13 (2014) 970–978, https://doi.org/10.1038/nmat4009.

[21] T.A. Krouskop, T.M. Wheeler, F. Kallel, B.S. Garra, T. Hall, Elastic moduli of breast and prostate tissues under compression, Ultrason. Imag. 20 (1998) 260–274, https://doi.org/10.1177/016173469802000403.

[22] K. Hoyt, B. Castaneda, M. Zhang, P. Nigwekar, P.A. di Sant'agnese, J.V. Joseph, J. Strang, D.J. Rubens, K.J. Parker, Tissue elasticity properties as biomarkers for prostate cancer, Canc. Biomarkers 4 (2008) 213–225, https://doi.org/10.3233/cbm-2008-44-505.

[23] B.-M. Ahn, J. Kim, L. Ian, K.-H. Rha, H.-J. Kim, Mechanical property characterization of prostate cancer using a minimally motorized indenter in an ex vivo indentation experiment, Urology 76 (2010) 1007–1011, https://doi.org/10.1016/j.urology.2010.02.025.

[24] M. Lekka, D. Gil, K. Pogoda, J. Dulińska-Litewka, R. Jach, J. Gostek, O. Klymenko, S. Prauzner-Bechcicki, Z. Stachura, J. Wiltowska-Zuber, K. Okoń, P. Laidler, Cancer cell detection in tissue sections using AFM, Arch. Biochem. Biophys. 518 (2012) 151–156, https://doi.org/10.1016/j.abb.2011.12.013.

[25] E.C. Faria, N. Ma, E. Gazi, P. Gardner, M. Brown, N.W. Clarke, R.D. Snook, Measurement of elastic properties of prostate cancer cells using AFM, Analyst 133 (2008) 1498–1500, https://doi.org/10.1039/b803355b.

[26] S.E. Cross, Y.-S. Jin, J. Rao, J.K. Gimzewski, Nanomechanical analysis of cells from cancer patients, Nat. Nanotechnol. 2 (2007) 780–783, https://doi.org/10.1038/nnano.2007.388.

[27] J. Guck, S. Schinkinger, B. Lincoln, F. Wottawah, S. Ebert, M. Romeyke, D. Lenz, H.M. Erickson, R. Ananthakrishnan, D. Mitchell, J. Käs, S. Ulvick, C. Bilby, Optical deformability as an inherent cell marker for testing malignant transformation and metastatic competence, Biophys. J. 88 (2005) 3689–3698, https://doi.org/10.1529/biophysj.104.045476.

[28] J. Rother, H. Nöding, I. Mey, A. Janshoff, Atomic force microscopy-based microrheology reveals significant differences in the viscoelastic response between malign and benign cell lines, Open Biol. 4 (2014) 140046, https://doi.org/10.1098/rsob.140046.

[29] V. Swaminathan, K. Mythreye, E.T. O'Brien, A. Berchuck, G.C. Blobe, R. Superfine, Mechanical stiffness grades metastatic potential in patient tumor cells and in cancer cell lines, Canc. Res. 71 (2011) 5075–5080, https://doi.org/10.1158/0008-5472.can-11-0247.

[30] W. Xu, R. Mezencev, B. Kim, L. Wang, J. McDonald, T. Sulchek, Cell stiffness is a biomarker of the metastatic potential of ovarian cancer cells, PloS One 7 (2012), e46609, https://doi.org/10.1371/journal.pone.0046609.

[31] D.B. Agus, J.F. Alexander, W. Arap, S. Ashili, J.E. Aslan, R.H. Austin, V. Backman, K.J. Bethel, R. Bonneau, W.-C. Chen, C. Chen-Tanyolac, N.C. Choi, S.A. Curley, M. Dallas, D. Damania, P.C.W. Davies, P. Decuzzi, L. Dickinson, L. Estevez-Salmeron, V. Estrella, M. Ferrari, C. Fischbach, J. Foo, S.I. Fraley, C. Frantz, A. Fuhrmann, P. Gascard, R.A. Gatenby, Y. Geng, S. Gerecht, R.J. Gillies, B. Godin, W.M. Grady, A. Greenfield, C. Hemphill, B.L. Hempstead, A. Hielscher, W.D. Hillis, E.C. Holland, A. Ibrahim-Hashim, T. Jacks, R.H. Johnson, A. Joo, J.E. Katz, L. Kelbauskas, C. Kesselman, M.R. King, K. Konstantopoulos, C.M. Kraning-Rush, P. Kuhn, K. Kung, B. Kwee, J.N. Lakins, G. Lambert, D. Liao, J.D. Licht, J.T. Liphardt, L. Liu, M.C. Lloyd, A. Lyubimova, P. Mallick, J. Marko, O.J.T. McCarty, D.R. Meldrum, F. Michor, S.M. Mumenthaler, V. Nandakumar, T.V. O'Halloran, S. Oh, R. Pasqualini, M.J. Paszek, K.G. Philips, C.S. Poultney, K. Rana, C.A. Reinhart-King, R. Ros, G.L. Semenza, P. Senechal, M.L. Shuler, S. Srinivasan, J.R. Staunton, Y. Stypula, H. Subramanian, T.D. Tlsty, G.W. Tormoen, Y. Tseng, A. van Oudenaarden, S.S. Verbridge, J.C. Wan, V.M. Weaver, J. Widom, C. Will, D. Wirtz, J. Wojtkowiak, P.-H. Wu, The Physical Sciences - oncology Centers Network, A physical sciences network characterization of non-tumorigenic and metastatic cells, Sci. Rep. 3 (2013) 1449, https://doi.org/10.1038/srep01449.

[32] E. Moeendarbary, A.R. Harris, Cell mechanics: principles, practices, and prospects, Wiley Interdiscip. Rev. Syst. Biol. Med. 6 (2014) 371–388, https://doi.org/10.1002/wsbm.1275.

[33] P.-H. Wu, D.R.-B. Aroush, A. Asnacios, W.-C. Chen, M.E. Dokukin, B.L. Doss, P. Durand-Smet, A. Ekpenyong, J. Guck, N.V. Guz, P.A. Janmey, J.S.H. Lee, N.M. Moore, A. Ott, Y.-C. Poh, R. Ros, M. Sander, I. Sokolov, J.R. Staunton, N. Wang, G. Whyte, D. Wirtz, A comparison of methods to assess cell mechanical properties, Nat. Methods 15 (2018) 491–498, https://doi.org/10.1038/s41592-018-0015-1.

[34] M. Krieg, G. Fläschner, D. Alsteens, B.M. Gaub, W.H. Roos, G.J.L. Wuite, H.E. Gaub, C. Gerber, Y.F. Dufrêne, D.J. Müller, Atomic force microscopy-based mechanobiology, Nat. Rev. Phys. 1 (2019) 41–57, https://doi.org/10.1038/s42254-018-0001-7.

[35] O. Otto, P. Rosendahl, A. Mietke, S. Golfier, C. Herold, D. Klaue, S. Girardo, S. Pagliara, A. Ekpenyong, A. Jacobi, M. Wobus, N. Töpfner, U.F. Keyser, J. Mansfeld, E. Fischer-Friedrich, J. Guck, Real-time deformability cytometry: on-the-fly cell mechanical phenotyping, Nat. Methods 12 (2015) 199–202, https://doi.org/10.1038/nmeth.3281.

[36] M.G. Lawrence, R.A. Taylor, R. Toivanen, J. Pedersen, S. Norden, D.W. Pook, M. Frydenberg, M.M. Papargiris, B. Niranjan, M.G. Richards, H. Wang, A.T. Collins, N.J. Maitland, G.P. Risbridger, A preclinical xenograft model of prostate cancer using human tumors, Nat. Protoc. 8 (2013) 836–848, https://doi.org/10.1038/nprot.2013.043.

[37] A.K. Clark, A.V. Taubenberger, R.A. Taylor, B. Niranjan, Z.Y. Chea, E. Zotenko, S. Sieh, J.S. Pedersen, S. Norden, M. Frydenberg, J.P. Grummet, D.W. Pook, C. Stirzaker, S.J. Clark, M.G. Lawrence, S.J. Ellem, D.W. Hutmacher, G.P. Risbridger, A bioengineered microenvironment to quantitatively measure the tumorigenic properties of cancer-associated fibroblasts in human prostate cancer, Biomaterials 34 (2013) 4777–4785, https://doi.org/10.1016/j.biomaterials.2013.03.005.

[38] E.V. Nguyen, B.A. Pereira, M.G. Lawrence, X. Ma, R.J. Rebello, H. Chan, B. Niranjan, Y. Wu, S. Ellem, X. Guan, J. Wu, J.N. Skhinas, T.R. Cox, G.P. Risbridger, R.A. Taylor, N.L. Lister, R.J. Daly, Proteomic profiling of human prostate cancer-associated fibroblasts (CAF) reveals LOXL2-dependent regulation of the tumor microenvironment, Mol. Cell. Proteomics 18 (2019) 1410–1427, https://doi.org/10.1074/mcp.ra119.001496.

[39] R. Pidsley, M.G. Lawrence, E. Zotenko, B. Niranjan, A. Statham, J. Song, R.M. Chabanon, W. Qu, H. Wang, M. Richards, S.S. Nair, N.J. Armstrong, H.T. Nim, M. Papargiris, P. Balanathan, H. French, T. Peters, S. Norden, A. Ryan, J. Pedersen, J. Kench, R.J. Daly, L.G. Horvath, P. Stricker, M. Frydenberg, R.A. Taylor, C. Stirzaker, G.P. Risbridger, S.J. Clark, Enduring epigenetic landmarks define the

cancer microenvironment, Genome Res. (2018), https://doi.org/10.1101/gr.229070.117.

[40] S.J. Ellem, R.A. Taylor, L. Furic, O. Larsson, M. Frydenberg, P. David, J. Pedersen, B. Cawsey, A. Trotta, E. Need, B. Grant, P. Risbridger Gail, A pro-tumourigenic loop at the human prostate tumour interface orchestrated by oestrogen, CXCL12 and mast cell recruitment, J. Pathol. 234 (2014) 86–98, https://doi.org/10.1002/path.4386.

[41] M.G. Lawrence, R. Pidsley, B. Niranjan, M. Papargiris, B.A. Pereira, M. Richards, L. Teng, S. Norden, A. Ryan, M. Frydenberg, C. Stirzaker, R.A. Taylor, G.P. Risbridger, S.J. Clark, Alterations in the methylome of the stromal tumour microenvironment signal the presence and severity of prostate cancer, Clin. Epigenet. 12 (2020) 48, https://doi.org/10.1186/s13148-020-00836-2.

[42] M.P. Chhaya, F.P.W. Melchels, B.M. Holzapfel, J.G. Baldwin, D.W. Hutmacher, Sustained regeneration of high-volume adipose tissue for breast reconstruction using computer aided design and biomanufacturing, Biomaterials 52 (2015) 551–560, https://doi.org/10.1016/j.biomaterials.2015.01.025.

[43] J. Franco-Barraza, D.A. Beacham, M.D. Amatangelo, E. Cukierman, Preparation of extracellular matrices produced by cultured and primary fibroblasts, Curr. Protoc. Cell Biol. 71 (2016), https://doi.org/10.1002/cpcb.2.

[44] H. Hertz, Ueber die Berührung fester elastischer Körper, J. für die Reine Angewandte Math. (Crelle's J.) (1882) (1882) 156–171, https://doi.org/10.1515/crll.1882.92.156.

[45] I.N. Sneddon, The relation between load and penetration in the axisymmetric boussinesq problem for a punch of arbitrary profile, Int. J. Eng. Sci. 3 (1965) 47–57, https://doi.org/10.1016/0020-7225(65)90019-4.

[46] M. Glaubitz, N. Medvedev, D. Pussak, L. Hartmann, S. Schmidt, C.A. Helm, M. Delcea, A novel contact model for AFM indentation experiments on soft spherical cell-like particles, Soft Matter 10 (2014) 6732, https://doi.org/10.1039/c4sm00788c.

[47] P. Rosendahl, K. Plak, A. Jacobi, M. Kraeter, N. Toepfner, O. Otto, C. Herold, M. Winzi, M. Herbig, Y. Ge, S. Girardo, K. Wagner, B. Baum, J. Guck, Real-time fluorescence and deformability cytometry, Nat. Methods 15 (2018) 355–358, https://doi.org/10.1038/nmeth.4639.

[48] D.W. Huang, B.T. Sherman, R.A. Lempicki, Systematic and integrative analysis of large gene lists using DAVID bioinformatics resources, Nat. Protoc. 4 (2009) 44–57, https://doi.org/10.1038/nprot.2008.211.

[49] D.W. Huang, B.T. Sherman, R.A. Lempicki, Bioinformatics enrichment tools: paths toward the comprehensive functional analysis of large gene lists, Nucleic Acids Res. 37 (2009) 1–13, https://doi.org/10.1093/nar/gkn923.

[50] The Gene Ontology Consortium, The gene ontology resource: 20 years and still GOing strong, Nucleic Acids Res. 47 (2019) D330–D338, https://doi.org/10.1093/nar/gky1055.

[51] M. Ashburner, C.A. Ball, J.A. Blake, D. Botstein, H. Butler, J.M. Cherry, A.P. Davis, K. Dolinski, S.S. Dwight, J.T. Eppig, M.A. Harris, D.P. Hill, L. Issel-Tarver, A. Kasarskis, S. Lewis, J.C. Matese, J.E. Richardson, M. Ringwald, G.M. Rubin, G. Sherlock, Gene Ontology: tool for the unification of biology, Nat. Genet. 25 (2000) 25–29, https://doi.org/10.1038/75556.

[52] The UniProt Consortium, UniProt: a worldwide hub of protein knowledge, Nucleic Acids Res. 47 (2019) D506–D515, https://doi.org/10.1093/nar/gky1049.

[53] M. Kanehisa, KEGG: kyoto encyclopedia of genes and genomes, Nucleic Acids Res. 28 (2000) 27–30, https://doi.org/10.1093/nar/28.1.27.

[54] R Core Team, R: A Language and Environment for Statistical Computing, 2013. Vienna, Austria, https://www.R-project.org/.

[55] W. Walter, F. Sánchez-Cabo, M. Ricote, GOplot: an R package for visually combining expression data with functional analysis: Fig. 1, Bioinformatics 31 (2015) 2912–2914, https://doi.org/10.1093/bioinformatics/btv300.

[56] R. Rezakhaniha, A. Agianniotis, J.T.C. Schrauwen, A. Griffa, D. Sage, C.V.C. Bouten, F.N. van de Vosse, M. Unser, N. Stergiopulos, Experimental investigation of collagen waviness and orientation in the arterial adventitia using confocal laser scanning microscopy, Biomech. Model. Mechanobiol. 11 (2012) 461–473, https://doi.org/10.1007/s10237-011-0325-z.

[57] J. Schindelin, I. Arganda-Carreras, E. Frise, V. Kaynig, M. Longair, T. Pietzsch, S. Preibisch, C. Rueden, S. Saalfeld, B. Schmid, J.-Y. Tinevez, D.J. White, V. Hartenstein, K. Eliceiri, P. Tomancak, A. Cardona, Fiji: an open-source platform for biological-image analysis, Nat. Methods 9 (2012) 676–682, https://doi.org/10.1038/nmeth.2019.

[58] R. Lotufo, A. Falcao, The ordered queue and the optimality of the watershed approaches, in: J. Goutsias, L. Vincent, D.S. Bloomberg (Eds.), Mathematical Morphology and its Applications to Image and Signal Processing, Springer US, Boston, MA, 2000, pp. 341–350, https://doi.org/10.1007/0-306-47025-X_37.

[59] D. Legland, I. Arganda-Carreras, P. Andrey, MorphoLibJ: integrated library and plugins for mathematical morphology with ImageJ, Bioinformatics (2016) 3532–3534, https://doi.org/10.1093/bioinformatics/btw413.

[60] S. Bolte, F.P. Cordelières, A guided tour into subcellular colocalization analysis in light microscopy, J. Microsc. 224 (2006) 213–232, https://doi.org/10.1111/j.1365-2818.2006.01706.x.

[61] H. Wickham, M. Averick, J. Bryan, W. Chang, L.D. McGowan, R. François, G. Grolemund, A. Hayes, L. Henry, J. Hester, M. Kuhn, T.L. Pedersen, E. Miller, S.M. Bache, K. Müller, J. Ooms, D. Robinson, D.P. Seidel, V. Spinu, K. Takahashi, D. Vaughan, C. Wilke, K. Woo, H. Yutani, Welcome to the tidyverse, J. Open Sour. Softw. 4 (2019) 1686, https://doi.org/10.21105/joss.01686.

[62] C. Fresno, E.A. Fernández, RDAVIDWebService: a versatile R interface to DAVID, Bioinformatics 29 (2013) 2810–2811, https://doi.org/10.1093/bioinformatics/btt487.

[63] D. Bates, M. Mächler, B. Bolker, S. Walker, Fitting linear mixed-effects models using lme4, J. Stat. Software 67 (2015) 1–48, https://doi.org/10.18637/jss.v067.i01.

[64] M. Herbig, A. Mietke, P. Müller, O. Otto, Statistics for real-time deformability cytometry: clustering, dimensionality reduction, and significance testing, Biomicrofluidics 12 (2018), https://doi.org/10.1063/1.5027197.

[65] F. Calvo, N. Ege, A. Grande-Garcia, S. Hooper, R.P. Jenkins, S.I. Chaudhry, K. Harrington, P. Williamson, E. Moeendarbary, G. Charras, E. Sahai, Mechanotransduction and YAP-dependent matrix remodelling is required for the generation and maintenance of cancer-associated fibroblasts, Nat. Cell Biol. 15 (2013) 637–646, https://doi.org/10.1038/ncb2756.

[66] Y. Ling, C. Li, K. Feng, S. Palmer, P.L. Appleton, S. Lang, D. McGloin, Z. Huang, G. Nabi, Second harmonic generation (SHG) imaging of cancer heterogeneity in ultrasound guided biopsies of prostate in men suspected with prostate cancer, J. Biophot. 10 (2017) 911–918, https://doi.org/10.1002/jbio.201600090.

[67] M.J. Paszek, N. Zahir, K.R. Johnson, J.N. Lakins, G.I. Rozenberg, A. Gefen, C.A. Reinhart-King, S.S. Margulies, M. Dembo, D. Boettiger, D.A. Hammer, V.M. Weaver, Tensional homeostasis and the malignant phenotype, Canc. Cell 8 (2005) 241–254, https://doi.org/10.1016/j.ccr.2005.08.010.

[68] K.R. Leventhal, H. Yu, L. Kass, J.N. Lakins, M. Egeblad, J.T. Erler, S.F.T. Fong, K. Csiszar, A. Giaccia, W. Weninger, M. Yamauchi, D.L. Gasser, V.M. Weaver, Matrix crosslinking forces tumor progression by enhancing integrin signaling, Cell 139 (2009) 891–906, https://doi.org/10.1016/j.cell.2009.10.027.

[69] A.S. Zeiger, F.C. Loe, R. Li, M. Raghunath, K.J. Van Vliet, Macromolecular crowding directs extracellular matrix organization and mesenchymal stem cell behavior, PloS One 7 (2012), e37904, https://doi.org/10.1371/journal.pone.0037904.

[70] M. Gupta, B.R. Sarangi, J. Deschamps, Y. Nematbakhsh, A. Callan-Jones, F. Margadant, R.-M. Mège, C.T. Lim, R. Voituriez, B. Ladoux, Adaptive rheology and ordering of cell cytoskeleton govern matrix rigidity sensing, Nat. Commun. 6 (2015) 1–9, https://doi.org/10.1038/ncomms8525.

[71] A.X. Cartagena-Rivera, J.S. Logue, C.M. Waterman, R.S. Chadwick, Actomyosin cortical mechanical properties in nonadherent cells determined by atomic force microscopy, biophys, J 110 (2016) 2528–2539, https://doi.org/10.1016/j.bpj.2016.04.034.

[72] R. Kumar, S. Saha, B. Sinha, Cell spread area and traction forces determine myosin-II-based cortex thickness regulation, Biochim. Biophys. Acta Mol. Cell Res. 1866 (2019) 118516, https://doi.org/10.1016/j.bbamcr.2019.07.011.

[73] A. Stylianou, V. Gkretsi, T. Stylianopoulos, Transforming growth factor-β modulates pancreatic cancer associated fibroblasts cell shape, stiffness and invasion, Biochim. Biophys. Acta Gen. Subj. 1862 (2018) 1537–1546, https://doi.org/10.1016/j.bbagen.2018.02.009.

[74] A. Stylianou, V. Gkretsi, M. Louca, L.C. Zacharia, T. Stylianopoulos, Collagen content and extracellular matrix cause cytoskeletal remodelling in pancreatic fibroblasts, J. R. Soc. Interface (2019) 16, https://doi.org/10.1098/rsif.2019.0226.

[75] M.B. Ginzberg, R. Kafri, M. Kirschner, On being the right (cell) size, Science 348 (2015), https://doi.org/10.1126/science.124507.

[76] F.-X. Yu, B. Zhao, K.-L. Guan, Hippo pathway in organ size control, tissue homeostasis, and cancer, Cell 163 (2015) 811–828, https://doi.org/10.1016/j.cell.2015.10.044.

[77] N. Perez Gonzalez, J. Tao, N.D. Rochman, D. Vig, E. Chiu, D. Wirtz, S.X. Sun, Cell tension and mechanical regulation of cell volume, MBoC 29 (2018), https://doi.org/10.1091/mbc.e18-04-0213.

[78] S. Piccolo, S. Dupont, M. Cordenonsi, The biology of YAP/TAZ: hippo signaling and beyond, Physiol. Rev. 94 (2014) 1287–1312, https://doi.org/10.1152/physrev.00005.2014.

[79] D.K. Kim, E.K. Kim, D.-W. Jung, J. Kim, Cytoskeletal alteration modulates cancer cell invasion through RhoA-YAP signaling in stromal fibroblasts, PloS One 14 (2019), https://doi.org/10.1371/journal.pone.0214553.

[80] L. Wullkopf, A.-K.V. West, N. Leijnse, T.R. Cox, C.D. Madsen, L.B. Oddershede, J.T. Erler, Cancer cells` ability to mechanically adjust to extracellular matrix stiffness correlates with their invasive potential, MBoC 29 (2018) 2378–2385, https://doi.org/10.1091/mbc.e18-05-0319.

[81] C.A. Brunner, A. Ehrlicher, B. Kohlstrunk, D. Knebel, J.A. Käs, M. Goegler, Cell migration through small gaps, Eur. Biophys. J. 35 (2006) 713–719, https://doi.org/10.1007/s00249-006-0079-1.

[82] K. Wolf, P. Friedl, Molecular mechanisms of cancer cell invasion and plasticity, Br. J. Dermatol. 154 (Suppl 1) (2006) 11–15, https://doi.org/10.1111/j.1365-2133.2006.07231.x.

[83] M. Cascione, V. De Matteis, C.C. Toma, S. Leporatti, Morphomechanical alterations induced by transforming growth factor-β1 in epithelial breast cancer cells, Cancers 10 (2018), https://doi.org/10.3390/cancers10070234.

[84] K. Hosseini, A. Taubenberger, C. Werner, E. Fischer-Friedrich, EMT-induced Cell Mechanical Changes Enhance Mitotic Rounding Strength, BioRxiv (2019), https://doi.org/10.1101/598052.

[85] L.D. Osborne, G.Z. Li, T. How, E.T. O'Brien, G.C. Blobe, R. Superfine, K. Mythreye, TGF-β regulates LARG and GEF-H1 during EMT to affect stiffening response to force and cell invasion, MBoC 25 (2014) 3528–3540, https://doi.org/10.1091/mbc.e14-05-1015.

[86] D.A. Fletcher, R.D. Mullins, Cell mechanics and the cytoskeleton, Nature 463 (2010) 485–492, https://doi.org/10.1038/nature08908.

[87] B.L. Doss, M. Pan, M. Gupta, G. Grenci, R.-M. Mège, C.T. Lim, M.P. Sheetz, R. Voituriez, B. Ladoux, Cell response to substrate rigidity is regulated by active and passive cytoskeletal stress, Proc. Natl. Acad. Sci. U.S.A. (2020), https://doi.org/10.1073/pnas.1917555117.

[88] E.L. Baker, R.T. Bonnecaze, M.H. Zaman, Extracellular matrix stiffness and architecture govern intracellular rheology in cancer, Biophys. J. 97 (2009) 1013–1021, https://doi.org/10.1016/j.bpj.2009.05.054.

[89] J. Solon, I. Levental, K. Sengupta, P.C. Georges, P.A. Janmey, Fibroblast adaptation and stiffness matching to soft elastic substrates, Biophys. J. 93 (2007) 4453–4461, https://doi.org/10.1529/biophysj.106.101386.

[90] J. Bauer, M.A.B. Emon, J.J. Staudacher, A.L. Thomas, J. Zessner-Spitzenberg, G. Mancinelli, N. Krett, M.T. Saif, B. Jung, Increased stiffness of the tumor microenvironment in colon cancer stimulates cancer associated fibroblast-mediated prometastatic activin A signaling, Sci. Rep. 10 (2020), https://doi.org/10.1038/s41598-019-55687-6.

[91] G. Ayala, J.A. Tuxhorn, T.M. Wheeler, A. Frolov, P.T. Scardino, M. Ohori, M. Wheeler, J. Spitler, D.R. Rowley, Reactive stroma as a predictor of biochemical-free recurrence in prostate cancer, Clin. Canc. Res. 9 (2003) 4792–4801.

[92] Z. Jia, Y. Wang, A. Sawyers, H. Yao, F. Rahmatpanah, X.-Q. Xia, Q. Xu, R. Pio, T. Turan, J.A. Koziol, S. Goodison, P. Carpenter, J. Wang-Rodriquez, A. Simoneau, F. Meyskens, M. Sutton, W. Lernhardt, T. Beach, J. Monforte, M. McClelland, D. Mercola, Diagnosis of prostate cancer using differentially expressed genes in stroma, Canc. Res. 71 (2011) 2476–2487, https://doi.org/10.1158/0008-5472.can-10-2585.